J. Fluid Mech. (1997), *vol.* 341, *pp.* 317–341. Printed in the United Kingdom

Nonlinear evolution and secondary instabilities of Marangoni convection in a liquid–gas system with deformable interface

By A. A. GOLOVIN[1]†, A. A. NEPOMNYASHCHY[2,3] AND L. M. PISMEN[1,3]

[1]Department of Chemical Engineering,
[2]Department of Mathematics,
[3]Minerva Centre for Non-linear Physics of Complex Systems,
Technion, Haifa 32000, Israel

(Received 11 April 1996 and in revised form 3 February 1997)

The paper presents a theory of nonlinear evolution and secondary instabilities in Marangoni (surface-tension-driven) convection in a two-layer liquid–gas system with a deformable interface, heated from below. The theory takes into account the motion and convective heat transfer both in the liquid and in the gas layers. A system of nonlinear evolution equations is derived that describes a general case of slow long-scale evolution of a short-scale hexagonal Marangoni convection pattern near the onset of convection, coupled with a long-scale deformational Marangoni instability. Two cases are considered: (i) when interfacial deformations are negligible; and (ii) when they lead to a specific secondary instability of the hexagonal convection.

In case (i), the extent of the subcritical region of the hexagonal Marangoni convection, the type of the hexagonal convection cells, selection of convection patterns – hexagons, rolls and squares – and transitions between them are studied, and the effect of convection in the gas phase is also investigated. Theoretical predictions are compared with experimental observations.

In case (ii), the interaction between the short-scale hexagonal convection and the long-scale deformational instability, when both modes of Marangoni convection are excited, is studied. It is shown that the short-scale convection suppresses the deformational instability. The latter can appear as a secondary long-scale instability of the short-scale hexagonal convection pattern. This secondary instability is shown to be either monotonic or oscillatory, the latter leading to the excitation of deformational waves, propagating along the short-scale hexagonal convection pattern and modulating its amplitude.

1. Introduction

Marangoni convection is the motion of a liquid caused by gradients of surface tension at a liquid–liquid or liquid–gas interface. These gradients usually appear in the course of heat or mass transfer due to the dependence of surface (interfacial) tension on temperature or concentration of the transferring substance. This type of convection is ubiquitous in technological processes of chemical and materials

† Present address: Department of Engineering Sciences and Applied Mathematics, Northwestern University, Evanston, IL 60208-3100, USA.

engineering, as well as in various space lab techniques where, under conditions of microgravity, surface tension gradients become a most important driving force of fluid motion.

In a large number of practical situations, Marangoni convection is generated by heat or mass transfer across the liquid layer(s). If mass or heat transfer goes from below to above, there exist two monotonic modes of Marangoni instability (Smith 1966; Takashima 1981). One mode is caused purely by surface tension gradients leading to the formation of a cellular convective structure; deformations of the free liquid surface are slaved to this cellular convective motion, and are usually negligible. The other mode is connected with deformations of the free surface governed also by gravity and capillary forces. Unless the characteristic time of diffusion across the system is small in comparison with the characteristic time of heat/mass exchange with the environment, these two modes have different characteristic spatial scales: the 'deformationless' mode yields convective motions on the scale of the liquid layer depth, while the spatial scale of convection generated by the deformational mode of Marangoni instability is much larger than the depth of the liquid layer; the former will further be called a *short-scale* mode and the latter a *long-scale* mode.

Hitherto, a large number of studies have been devoted to a separate nonlinear evolution of a single mode of Marangoni instability, either short or longscale. However, when the thresholds of the short-scale deformationless Marangoni instability and the long-scale deformational one are close to each other, these two types of convection can coexist and interact. This interaction has been studied theoretically by Golovin, Nepomnyashchy & Pismen (1994), Kazhdan *et al.* (1995) and Golovin *et al.* (1997) in a model one-dimensional roll-cell Marangoni convection in a one-layer system. In real systems, however, Marangoni convection occurs in the form of hexagonal convection cells. This hexagonal convection pattern can interact with two-dimensional long-scale surface deformations, as has been observed in experiment by Van Hook *et al.* (1995), and there is as yet no theory describing this realistic case.

The existing theories, describing nonlinear evolution of *short-scale* Marangoni convection patterns, have a common simplification: they consider convection in the liquid layer only, and model the effect of the adjacent gas phase by introducing an effective empirical parameter – the Biot number – characterizing the intensity of heat or mass transfer between the liquid and the gas. Such an approach will be referred to as a *one-layer* one, and the systems to which it is applied will be called one-layer systems. In many cases predictions of the one-layer approach are in a qualitative agreement with experimental observations. The Biot number can be well defined for the steady-state conditions: it is a simple function of the ratio of heat conductivities in the liquid and the gas layers, and of the ratio of the layers depths. When the steady state becomes unstable and convection sets in, the intensity of heat transfer in the gas phase substantially depends on perturbations of the temperature field there, produced both by thermal perturbations at the liquid–gas interface and by convection in the gas layer itself. Therefore, there are still certain difficulties in comparing the existing theories with experimental observations of liquid–gas systems, and it is important to investigate the effect of convection in the gas phase on the nonlinear evolution of short-scale Marangoni convection patterns.

In the present paper we shall develop a theory that will describe the nonlinear evolution and selection of two-dimensional planforms in three-dimensional short-scale Marangoni convection in a realistic two-layer liquid–gas system and will take into account the convective motion and heat transfer both in the liquid and in the gas phase. Within this realistic two-layer approach, we shall also provide a theory describing the

interaction between the short-scale hexagonal convection pattern and the long-scale deformational instability†. The predictions of the theory will be compared with recent experimental observations (Van Hook *et al.* 1995; Nitschke & Thess 1995).

2. Basic equations and boundary conditions

We consider a two-layer liquid–gas system with a deformable liquid–gas interface, bounded from below and from above by rigid plates. The system is heated from below, and the rigid plates are perfect thermal conductors having constant temperatures T_{10} at the bottom and T_{20} at the top, $T_{10} > T_{20}$. The liquid–gas surface tension depends linearly on temperature; other physical properties are assumed constant. We also neglect the effect of buoyancy, and consider the Marangoni mechanism of convective instability to be predominant, i.e. we suppose that either temperature dependence of the fluid density is very weak, or that the liquid layer is sufficiently thin, so that the Rayleigh number, decreasing with the liquid layer depth much faster than the Marangoni number, is far below the threshold of the buoyancy-driven convection.

Hydrodynamics and heat transfer in both phases, as well as interfacial dynamics, are described by the following system of dimensionless equations and boundary conditions:

$$\frac{1}{Pr}(\partial_t + \boldsymbol{v}_1\cdot\nabla + w_1\partial_z)\begin{Bmatrix}\boldsymbol{v}_1\\ w_1\end{Bmatrix} = -\begin{Bmatrix}\nabla p_1\\ \partial_z p_1\end{Bmatrix} + (\nabla^2+\partial_{zz})\begin{Bmatrix}\boldsymbol{v}_1\\ w_1\end{Bmatrix} - \begin{Bmatrix}0\\ G\end{Bmatrix}, \quad (2.1)$$

$$\frac{\rho}{Pr}(\partial_t + \boldsymbol{v}_2\cdot\nabla + w_2\partial_z)\begin{Bmatrix}\boldsymbol{v}_2\\ w_2\end{Bmatrix} = -\begin{Bmatrix}\nabla p_2\\ \partial_z p_2\end{Bmatrix} + \eta(\nabla^2+\partial_{zz})\begin{Bmatrix}\boldsymbol{v}_2\\ w_2\end{Bmatrix} - \begin{Bmatrix}0\\ \rho G\end{Bmatrix}, \quad (2.2)$$

$$\nabla\cdot\boldsymbol{v}_i + \partial_z w_i = 0, \qquad i = 1,2, \quad (2.3)$$

$$(\partial_t + \boldsymbol{v}_1\cdot\nabla + w_1\partial_z)\theta_1 = (\nabla^2+\partial_{zz})\theta_1, \quad (2.4)$$

$$(\partial_t + \boldsymbol{v}_2\cdot\nabla + w_2\partial_z)\theta_2 = \chi(\nabla^2+\partial_{zz})\theta_2, \quad (2.5)$$

$$z = 0: \qquad \boldsymbol{v}_1 = w_1 = 0, \qquad \theta_1 = 1; \quad (2.6)$$

$$z = 1+a: \qquad \boldsymbol{v}_2 = w_2 = \theta_2 = 0; \quad (2.7)$$

$$z = 1+h: \qquad \boldsymbol{v}_1 = \boldsymbol{v}_2, \qquad w_1 = w_2, \qquad h_t + \boldsymbol{v}_1\cdot\nabla h = w_1, \quad (2.8)$$

$$\theta_1 = \theta_2, \qquad \partial_z\theta_1 - \nabla h\cdot\nabla\theta_1 = \kappa(\partial_z\theta_2 - \nabla h\cdot\nabla\theta_2) \quad (2.9)$$

$$\boldsymbol{\Pi}:\boldsymbol{nn} = \nabla\cdot\left(\frac{\nabla h}{(1+(\nabla h)^2)^{1/2}}\right)(Ca - Ma\theta_1), \quad (2.10)$$

$$\boldsymbol{\Pi}:\boldsymbol{nt}_\alpha = Ma\frac{1}{(1+(\partial_\alpha h)^2)^{1/2}}(\partial_\alpha\theta_1 + \partial_z\theta_1\partial_\alpha h), \quad (2.11)$$

where x, y are the planar coordinates, z is the vertical coordinate with $z = 0$ at the bottom; ∇ is the two-dimensional planar gradient (∂_x, ∂_y), $\boldsymbol{v}$ is the two-dimensional velocity vector in the (x,y)-plane, w is the z-component of the velocity, $\theta = (T - T_{20})/(\Delta T)_0$ is the dimensionless temperature, p is pressure, h is the surface deformation, $\boldsymbol{\Pi}$ is the dimensionless stress tensor of the liquid, $\Pi_{jk} = -p_1\delta_{jk} + (\partial_k v_j + \partial_j v_k)$ $(j,k = x,y,z)$;

$$\boldsymbol{n} = \left(-\frac{\nabla h}{(1+(\nabla h)^2)^{1/2}}, \frac{1}{(1+(\nabla h)^2)^{1/2}}\right), \quad \boldsymbol{t}_\alpha = (\delta_{\alpha x}, \delta_{\alpha y}, \partial_\alpha h)/(1+(\partial_\alpha h)^2)^{1/2}$$

† Interaction between a *long-scale* hexagonal convection planform and the long-scale surface deformations in the case of Marangoni convection in a liquid–gas system with thermally nearly insulated boundaries has been studied by Hadji (1994, 1996) and by Golovin, Nepomnyashchy & Pismen (1995).

are the normal and tangential vectors at the interface, respectively, $\alpha = x, y$; $\rho = \rho_2/\rho_1$, $\eta = \eta_2/\eta_1$, $\kappa = \kappa_2/\kappa_1$, $\chi = \chi_2/\chi_1$, $a = L_2/L_1$, where subscripts $i = 1, 2$ correspond to the liquid and the gas phase, respectively. Here L_i is the depth of the phase i, ρ_i is the density, η_i is the dynamic viscosity, κ_i is the heat conductivity, χ_i is the thermal diffusivity, T is temperature, $(\Delta T)_0 = T_{10} - T_{20}$. In boundary conditions (2.10), (2.11) we neglected the stresses produced by the gas phase, since both the density and dynamic viscosity of gases can be considered negligible in comparison with those of liquids; we also omitted an insignificant constant pressure in the gas phase.

The following scaling is chosen: L_1 for spatial coordinates, L_1^2/χ_1 for time, χ_1/L_1 for velocity, $\eta_1\chi_1/L_1^2$ for pressure. The dimensionless parameters are: $Pr = \nu_1/\chi_1$ – Prandtl number of the liquid, $Ma = -(\partial\sigma/\partial T)L_1(\Delta T)_0/(\eta_1\chi_1)$ – Marangoni number (where the sign minus is inserted to make the Marangoni number positive, since, typically, the liquid–gas surface tension decreases with temperature) $G = g_0 L_1^3/(\nu_1\chi_1)$ – Galileo number, $Ca = \sigma L_1/(\eta_1\chi_1)$ – capillary number, where ν_1 is the kinematic viscosity of the liquid, σ is the liquid–gas interfacial tension, g_0 is the acceleration due to gravity. Note, that under usual conditions the Galileo and capillary numbers, G and Ca, are very large: e.g. for a 1 mm water layer at the room temperature and atmospheric pressure, $G = 6.8 \times 10^4$, $Ca = 5.1 \times 10^5$; for the 0.3 mm layer of 10 cS silicon oil, $G = 2.6 \times 10^2$, $Ca = 6.4 \times 10^3$.

3. Thresholds of Marangoni instability

The dimensionless parameter governing the instability induced by surface tension gradients is the Marangoni number Ma. A comprehensive linear stability analysis of Marangoni convection in a general case of a liquid–liquid system with deformable interface has been carried out by Smith (1966), Imaishi & Fujinawa (1974), Imaishi, Fujinawa & Tadaki (1980), Reichenbach & Linde (1981), and Simanovskii & Nepomnyashchy (1993). In the particular case of a liquid–gas system described by (2.1)–(2.11), the Marangoni convection results from a monotonic instability, and the neutral stability boundary $Ma(k, a, \kappa, \chi, G, Ca)$ usually has two minima: $Ma_s(a, \kappa, \chi, G, Ca)$ at $k \neq 0$, and $Ma_l(a, \kappa, G)$ at $k = 0$, corresponding to the onset of the short- and the long-scale convection, respectively (Simanovskii & Nepomnyashchy 1993).

Figure 1 shows typical neutral stability curves for a silicon oil–air system studied experimentally by Van Hook *et al.* (1995). It can be seen that in a given liquid–gas system, the desired type of Marangoni instability can be obtained experimentally by varying geometrical parameters, either the depth of the liquid layer (figure 1*a*) or the width of the gas gap (figure 1*b*). Note that the type of the neutral stability curves can differ from that shown in figure 1, if the gas gap is considerably thicker than the liquid layer, so that $a^2/\chi \sim 1$. For typical experiments, $a \sim 1$, $\chi \sim 10^2$ and $a^2/\chi \ll 1$. (Simanovskii & Nepomnyashchy 1993).

4. Evolution equations near Marangoni instability thresholds

In this section we consider a two-layer liquid–gas system with parameters adjusted in such a way that the two thresholds of different types of Marangoni convection are close to each other. We will derive a system of amplitude equations describing the evolution of a short-scale hexagonal convection pattern and its interaction with the long-scale deformational instability in the vicinity of the two thresholds. The derivation procedure is analogous to that used by Scanlon & Segel (1967), Cloot &

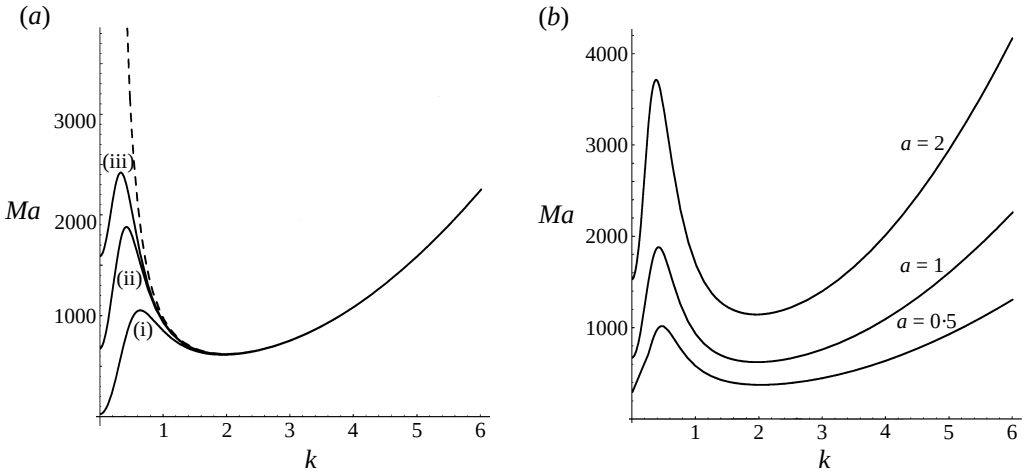

FIGURE 1. Neutral stability curves Ma(k) for the Marangoni instability in a silicon oil–air system (Van Hook *et al.* 1995) ($v_1 = 0.1$ cm^2 s^{-1}, $\kappa_1 = 1.42 \times 10^4$ erg cm^{-1} s^{-1} K^{-1}: (*a*) with $a = 1$ and various liquid layer depths: (i) 0.1 mm, (ii) 0.3 mm, (iii) 0.4 mm; dashed line corresponds to $G = Ca = \infty$ (no surface deformation), with $L = 0.4$ mm; (*b*) with $L = 0.3$ mm and different gas-to-liquid depths ratios.

Lebon (1984), Bragard & Lebon (1993), and Golovin *et al.* (1994). In this section, we present only basic steps of the nonlinear analysis and discuss certain details which are important for the particular case considered here and which are different from the previous studies.

In order to describe the nonlinear evolution of the short-scale hexagonal convection pattern coupled with long-scale slow surface deformations, we introduce a long-scale planar coordinate $\boldsymbol{R} = (X,\ Y) = \epsilon \boldsymbol{r} = (\epsilon x,\ \epsilon y)$, and two slow time variables, $\tau = \epsilon t,\ T = \epsilon^2 t$, where ϵ^2 is a small supercriticality parameter depending on Ma–Ma_s. We apply the following expansion:

$$\left.\begin{aligned} \boldsymbol{V}_j &= \epsilon \boldsymbol{V}_j^{(1)} + \epsilon^2 \boldsymbol{V}_j^{(2)} + \epsilon^3 \boldsymbol{V}_j^{(3)} + \ldots, \\ p_j &= p_{j0} + \epsilon p_j^{(1)} + \epsilon^2 p_j^{(2)} + \epsilon^3 p_j^{(3)} + \ldots, \\ \theta_j &= \theta_{j0} + \epsilon \theta_j^{(1)} + \epsilon^2 \theta_j^{(2)} + \epsilon^3 \theta_j^{(3)} + \ldots, \\ h &= \epsilon^2 H + \ldots, \\ Ma &= Ma_s + \epsilon Ma_1 + \epsilon^2 Ma_2 + \ldots, \\ \nabla &= \nabla + \epsilon \hat{\nabla} + \ldots, \\ \partial_t &= \epsilon \partial_\tau + \epsilon^2 \partial_T + \ldots, \end{aligned}\right\} \tag{4.1}$$

where $\boldsymbol{V}_j = (\boldsymbol{v}_j,\ w_j)$ is the three-dimensional velocity, $\hat{\nabla} = (\partial_X,\ \partial_Y)$ is the long-scale two-dimensional (planar) gradient, and the unperturbed temperature and pressure profiles in the steady state θ_{j0} and p_{j0} are

$$\left.\begin{aligned} &\theta_{10} = 1 - \beta_0 z, \quad \theta_{20} = \frac{1+a}{\kappa+a} - \frac{\beta_0}{\kappa} z, \quad \beta_0 = \frac{\kappa}{\kappa+a}, \\ &p_{10} = -Gz, \quad p_{20} = -G(1-\rho) - \rho G z. \end{aligned}\right\} \tag{4.2}$$

We use a uniform scaling for long-scale space coordinates since we are interested in the evolution of a hexagonal convection pattern, whose wave-vectors are locked by the resonant interaction condition $\boldsymbol{k}_1 + \boldsymbol{k}_2 + \boldsymbol{k}_3 = 0$. This condition restricts the allowed region of disturbances of the wave-vectors in the Fourier space near the

instability threshold to a narrower interval than that of a roll pattern, so that, instead of a non-uniform scaling for the X- and Y-coordinates introduced by Segel (1969) and Newell & Whitehead (1969), $X \sim \epsilon$, $Y \sim \epsilon^{1/2}$, a uniform scaling, $\boldsymbol{R} = \epsilon \boldsymbol{r}$, should be used (Pomeau 1986; Pismen & Nepomnyashchy 1993).

The scaling for h in (4.1) is determined by the fact that the Galileo and capillary numbers are usually very large, $G \sim 10^2$–10^4, $Ca \sim 10^5$. Otherwise, one would write $h = \epsilon h^{(1)} + \epsilon^2 H + \ldots$, where $h^{(1)}$ is the short-scale surface deformation caused by the short-scale Marangoni convection. However, $h^{(1)} \sim \epsilon/(G+Ca)$, and there is, therefore, a good reason to neglect short-scale surface deformations, setting $h^{(1)} \equiv 0$, and to take into account only the long-scale deformations of the liquid–gas interface H, which are of the order of ϵ^2 and which are responsible for the interaction with the mean heat flux and the mean flow generated by the short-scale convection. Such an approximation allows us to simplify further calculation of the nonlinear interaction coefficients by using the simplified eigenfunctions corresponding to the case of an undeformable interface, and with the linear instability threshold $Ma_s(a, \kappa, \chi)$ corresponding to infinite Galileo and capillary numbers. The surface deformation H should be taken into account when deriving the evolution equation governing the long-scale surface deformations interacting with the mean flow and the mean temperature field generated by the short-scale convection; at this stage, we will suggest that $G = O(1)$ and $Ca = O(\epsilon^{-2})$.

Applying expansions (4.1) to the Navier–Stokes equations (2.1), (2.2) and to the heat transport equations (2.4), (2.5), we obtain a set of linear inhomogeneous problems, the solvability conditions for which in subsequent orders of the expansion will give us evolution equations for the nonlinear Marangoni convection. The linear operator, the adjoint problem, and the solvability conditions in the subsequent orders of the perturbation theory are given in Appendix A.

In the lowest (linear) approximation, the hexagonal convection pattern is described by

$$\left.\begin{aligned} \boldsymbol{V}_j^{(1)} &= \frac{\mathrm{i}}{k_{cr}^2}\frac{\mathrm{d}\psi_j(z)}{\mathrm{d}z}\sum_{n=1}^{3}\boldsymbol{k}_n A_n(\boldsymbol{R}, T)\mathrm{e}^{\mathrm{i}\boldsymbol{k}_n\cdot\boldsymbol{r}} + \psi_j(z)\boldsymbol{e}_z\sum_{n=1}^{3}A_n(\boldsymbol{R}, T)\mathrm{e}^{\mathrm{i}\boldsymbol{k}_n\cdot\boldsymbol{r}} + \text{c.c.},\\ \theta_j^{(1)} &= \phi_j(z)\sum_{n=1}^{3}A_n(\boldsymbol{R}, T)\mathrm{e}^{\mathrm{i}\boldsymbol{k}_n\cdot\boldsymbol{r}} + \text{c.c.}, \end{aligned}\right\} \tag{4.3}$$

where $\psi_j(z)$, $\phi_j(z)$ are eigenfunctions obtained from the linear stability analysis in the case of an undeformable interface, $\boldsymbol{r} = (x, y)$ is the planar radius vector, $\boldsymbol{k}_n$ are the wave-vectors of the hexagonal pattern forming the resonant triad: $\boldsymbol{k}_1 + \boldsymbol{k}_2 + \boldsymbol{k}_3 = 0, |\boldsymbol{k}_n| = k_{cr}$, corresponding to the short-scale instability threshold Ma_s, and A_n are complex amplitudes undergoing slow long-scale evolution.

In the second order, the solvability condition gives the following system of equations for the amplitudes A_n:

$$\partial_\tau A_n = \gamma_0 Ma_1 A_n + \alpha A_l^* A_m^*, \quad n, l, m = 1, 2, 3. \tag{4.4}$$

The solutions of (4.4) are known, however, to blow up, and higher-order terms should be included in order to get a nonlinear saturation leading to a physically reasonable solution. In the formal derivation procedure we suppose that the quadratic terms $\alpha A_l^* A_m^*$ are small, and they should be taken into account only in the third order of the perturbation theory. The smallness of this term should be checked *a posteriori*. This procedure is equivalent to the Galerkin approximation which takes into account the

lowest modes generated by the quadratic nonlinearities of the Navier–Stokes and heat transport equations, with the subsequent adiabatic elimination of higher harmonics; these modes correspond to the wave-vectors $\boldsymbol{k}_l - \boldsymbol{k}_m$ with $l \neq m$ and $2\boldsymbol{k}_n$. Therefore, we have to accept $\partial_\tau = Ma_1 = 0$ and proceed to the third order of the perturbation theory.

The solution for $\boldsymbol{V}^{(2)}$ required for further derivations contains only terms corresponding to $\boldsymbol{k}_l - \boldsymbol{k}_m$ and $2\boldsymbol{k}_n$ (the resonant modes $\boldsymbol{k}_l + \boldsymbol{k}_m = -\boldsymbol{k}_n$ are formally related to the third order), whereas $\theta_j^{(2)}$ and $p_j^{(2)}$ have 'zero modes' which depend only on the long-scale horizontal coordinate $\boldsymbol{R}$ and slow time T, and describe the mean heat flux and the mean pressure field in the liquid and gas layers generated by the nonlinear convection effects. These zero modes depend on the interfacial deformation H and on the amplitudes of the short-scale convection A_n

$$\left.\begin{aligned} \theta_{j,0}^{(2)} &= \phi_{j,0H}^{(2)}(z)H + \phi_{j,0A}^{(2)}(z)\sum_{n=1}^{3}|A_n|^2, \\ p_{1,0}^{(2)} &= GH - Ca\hat{\nabla}^2 H - \frac{2}{Pr}\psi_1^2\sum_{n=1}^{3}|A_n|^2, \end{aligned}\right\} \tag{4.5}$$

where the functions $\phi_{j,0H}^{(2)}(z)$ and $\phi_{j,0A}^{(2)}(z)$ are expressed in terms of the functions $\psi_j(z)$ and $\phi_j(z)$.

In the third order, the solvability condition yields the following evolution equations for the amplitudes A_n of the short-scale hexagonal convection:

$$\begin{aligned} \partial_T A_n = \gamma_0(Ma - Ma_s)A_n + \delta(\boldsymbol{k}_n\cdot\hat{\nabla})^2 A_n + \alpha A_l^* A_m^* + \mathrm{i}\sum_{l,m\neq n}[A_l^*(\alpha_1\boldsymbol{k}_l + \beta_1\boldsymbol{k}_m)\cdot\hat{\nabla}A_m^*] \\ -\lambda_0|A_n|^2 A_n - \lambda_h(|A_l|^2 + |A_m|^2)A_n + \sigma_0 A_n H, \quad l,m,n = 1,2,3. \end{aligned} \tag{4.6}$$

Equations (4.6) generalize the standard amplitude equations describing the evolution of a hexagonal pattern near the instability threshold. They contain the quadratic terms with the amplitudes gradients (with coefficients α_1 and β_1) which include the terms introduced by Brand (1989) in the form $\mathrm{i}K_0[A_l^*(\boldsymbol{k}_m\cdot\nabla)A_m^* + A_m^*(\boldsymbol{k}_l\cdot\nabla)A_l^*]$, the terms in the form $\mathrm{i}Q_0[A_l^*(\boldsymbol{k}_l\cdot\nabla)A_m^* + A_m^*(\mathbf{k}_m\cdot\nabla)A_l^*]$ discussed by Gunaratne, Ouyang & Swinney (1994), as well as the terms derived by Kuznetsov, Nepomnyashchy & Pismen (1995) and by Pontes (1994) for the case of buoyancy-driven Boussinesq convection in the form $\mathrm{i}K_1[A_l^*(\boldsymbol{t}_m\cdot\nabla)A_m^* - A_m^*(\boldsymbol{t}_l\cdot\nabla)A_l^*]$, where $\boldsymbol{t}_n$ is a unit vector normal to $\boldsymbol{k}_n$. These generalized quadratic terms with the gradient of the amplitudes have been also recently obtained by Bragard & Velarde (1996) for the case of Marangoni convection in a one-layer system. Equations (4.6) also contain the additional nonlinear terms $\sigma_0 A_n H$ which reflect the influence of the long-scale surface deformation on the evolution of the short-scale Marangoni convection: the surface deformation locally changes the critical Marangoni number, yielding thereby a space–time-dependent supercriticality parameter $\gamma_0(Ma - Ma_s) + \sigma_0 H(\boldsymbol{R}, T)$. Coefficients in system (4.6) depend on the liquid Prandtl number, on the ratio of the heat transport coefficients in the gas and the liquid, and on the geometry of the system. The coefficients γ_0, δ, and the interaction coefficient σ_0 are always positive. Therefore, the long-scale surface elevations promote the development of the short-scale hexagonal convection. The coefficient of the quadratic resonant interaction α (as well as coefficients α_1 and β_1) can change its sign, resulting in the appearance of hexagonal cells with different directions of the fluid motion (see the next section).

System (4.6) should be supplemented by an evolution equation for the surface deformation H. This equation follows from the kinematic condition in the fourth order:

$$\partial_T H = -\int_0^1 \hat{\nabla}\cdot \boldsymbol{v}_{1,0}^{(3)}\,\mathrm{d}z, \tag{4.7}$$

where $\boldsymbol{v}_{1,0}^{(3)}$ is the horizontal component of the aperiodic mean flow appearing in the third order,

$$\boldsymbol{v}_{1,0}^{(3)} = \boldsymbol{A}z^2 + \boldsymbol{B}z + F_0(z)\sum_{n=1}^{3}\boldsymbol{k}_n(\boldsymbol{k}_n\cdot\hat{\nabla})|A_n|^2 - G_0(z)\sum_{n=1}^{3}\hat{\nabla}|A_n|^2, \tag{4.8}$$

where $F_0(z)$, $G_0(z)$ are computable functions of the vertical coordinate, and constants $\boldsymbol{A}$, $\boldsymbol{B}$ should be found from the Navier–Stokes equation (2.1) in the third order of the perturbation theory, and from the tangential stress boundary condition (2.11).

Finally, we obtain from (4.7) the following evolution equation for the surface deformation H:

$$\partial_T H = -\tfrac{1}{3}G\left(\frac{Ma_s}{Ma_l}-1\right)\hat{\nabla}^2 H - \tfrac{1}{3}Ca\hat{\nabla}^4 H + \sigma_1\sum_{i=1}^{3}(\boldsymbol{k}_i\cdot\hat{\nabla})^2|A_i|^2 + \sigma_2\sum_{i=1}^{3}\hat{\nabla}^2|A_i|^2, \tag{4.9}$$

with $Ma_s(a, \kappa, \chi)$ corresponding to the minimum of the neutral stability curve at $k \neq 0$ with $G = Ca = \infty$, and $Ma_l(a, \kappa, G) = \frac{2}{3}\,G(a+\kappa)^2(1+a)^{-1}\kappa^{-1}$.

The coefficients σ_1 and σ_2 in (4.9) depend on the physical and geometrical parameters of the system and turn out to be positive. These terms therefore reflect the stabilizing influence of the short-scale hexagonal convection pattern: it suppresses the deformational instability by intensifying the mean heat flux from the bottom to the top, thereby yielding additional long-scale surface tension gradients which tend to smooth the interface. Thus, system (4.6), (4.9) describes the nonlinear evolution of the short-scale hexagonal Marangoni convection pattern in the general case, when it interacts with the long-scale deformational mode of Marangoni instability.

Table 1 presents the values of the parameters of system (4.6) and (4.9) for some liquid–air systems with close thresholds Ma_s and Ma_l. All the coefficients in (4.6) and (4.9) are computed analytically and the computation is checked by the MATHEMATICA symbolic computations software package.

After rescaling $A \to \alpha A/\lambda_0$, $T \to \lambda_0 T/\alpha^2$, $\boldsymbol{R} \to k_{cr}(\delta\lambda_0)^{1/2}\boldsymbol{R}/\alpha$, $H \to \alpha^2 H/(\lambda_0\sigma)^{1/2}$, system (4.6), (4.9) can be rewritten in the following form:

$$\left.\begin{aligned}
&\partial_T A_n = \gamma A_n + (\boldsymbol{n}_n\cdot\hat{\nabla})^2 A_n + A_l^* A_m^* + \mathrm{i}\sum_{l,m\neq n}[A_l^*(a_1\boldsymbol{n}_l + b_1\boldsymbol{n}_m)\cdot\hat{\nabla}A_m^*]\\
&-|A_n|^2 A_n - \lambda(|A_l|^2 + |A_m|^2)A_n + A_n H,\ n,m,l = 1,2,3,\\
&\partial_T H = -\mu\hat{\nabla}^2 H - w\hat{\nabla}^4 H + s_1\sum_{n=1}^{3}(\mathbf{n}_n\cdot\hat{\nabla})^2|A_n|^2 + s_2\sum_{n=1}^{3}\hat{\nabla}^2|A_n|^2.
\end{aligned}\right\} \tag{4.10}$$

Here

$$\left.\begin{aligned}
&\boldsymbol{n}_n = \frac{\boldsymbol{k}_n}{k_{cr}},\quad \gamma = \gamma_0\frac{\lambda_0}{\alpha^2}(Ma - Ma_s),\quad (a_1, b_1) = \frac{(\alpha_1, \beta_1)}{(\delta\lambda_0)^{1/2}},\quad \lambda = \frac{\lambda_h}{\lambda_0},\\
&\mu = \tfrac{1}{3}G\frac{1}{\delta k_{cr}^2}\left(\frac{Ma_s}{Ma_l}-1\right),\quad w = \tfrac{1}{3}Ca\frac{\alpha^2}{k_{cr}^4\delta^2\lambda_0},\quad s_1 = \frac{\sigma_1\sigma_0}{\lambda_0\delta},\quad s_2 = \frac{\sigma_2\sigma_0}{\lambda_0\delta k_{cr}^2},
\end{aligned}\right\} \tag{4.11}$$

	Water, Pr=7	Ethanol, $Pr = 16.1$	Silicon oil[a], $Pr = 100$	Silicon oil[b], $Pr = 913$
L, mm	0.2	0.2	0.3	0.8
a	0.25	0.2	0.75	0.25
Ma_s	594.75	259.76	490.32	272.45
Ma_l	587.84	258.04	485.54	261.64
G	548.8	562.6	264.9	458.7
$Ca \times 10^{-3}$	101	414	6.41	1.46
$\gamma_0 \times 10^2$	1.054	2.977	1.368	2.743
δ	0.408	0.414	0.464	0.429
α	0.433	0.634	0.464	0.614
α_1	−0.167	−0.187	−0.16	−0.184
β_1	−0.119	−0.136	−0.15	−0.160
λ_0	0.332	0.368	0.284	0.352
λ_h	0.430	0.452	0.360	0.433
σ_0	30.95	24.19	18.76	24.4
$\sigma_1 \times 10^3$	5.72	2.74	0.391	0.047
σ_2	0.486	0.487	0.457	0.485

TABLE 1. Parameters in (4.6) and (4.9) corresponding to some liquid–air systems at the room temperature and atmospheric pressure: [a] used by Van Hook *et al.* (1995); [b] used by Koschmieder & Biggerstaff (1986).

System (4.10) generalizes a one-dimensional system, derived previously by Golovin *et al.* (1994), to a realistic case of interaction between a three-dimensional short-scale hexagonal convection pattern and two-dimensional long-scale interfacial deformations.

In conclusion of this section, let us concentrate on the ways of controlling the coefficients of system (4.10) in the experiment. The parameter γ is proportional to the deviation of the Marangoni number from the short-scale instability threshold, and it can be changed by varying the temperature difference between the bottom and the top plates. This is the only parameter depending on the intensity of heating. The parameter μ, being proportional to the difference between the two thresholds of Marangoni instability, $Ma_s - Ma_l$, depends mainly on the geometry of the system: on the depth of the liquid layer and on the gas-to-liquid depths ratio. Changing the depth of the liquid layer and keeping the gas-to-liquid depths ratio constant, one can vary the Galileo and capillary numbers only. This would allow one to change the value and the sign of the coefficients μ and w controlling the linear growth rate of the deformational instability, and would enable the study of different types of interaction between the short-scale hexagonal Marangoni convection and the long-scale interfacial deformations (see Golovin *et al.* 1994). Another possibility is to change dynamically the gas gap, within a single experimental run. Other parameters, however, will also change with the variation of the gas-to-liquid depths ratio a. Besides, all the coefficients of nonlinear interaction depend strongly on the Prandtl number of the liquid and on the ratios of transport coefficients κ, χ, ν. The important fact is that the coefficient of the resonant quadratic interaction α in system (4.6) also strongly depends on Pr and on a, κ, χ, ν, and can change its sign. This makes possible two types of hexagons with different directions of the fluid motion (see the next section).

5. Characteristics of a hexagonal pattern

A solution of eqs. (4.10) describing a regular hexagonal Marangoni convection pattern without surface deformation is

$$A_n = A_0 = \frac{1 + [1 + 4\gamma(1 + 2\lambda)]^{1/2}}{2(1 + 2\lambda)} \quad (\text{at } \alpha > 0), \quad H = 0. \tag{5.1}$$

This pattern is excited subcritically, at $\gamma > \gamma_{sub} = -1/(4(1+2\lambda))$, (when the Marangoni number exceeds a subcritical threshold, $Ma > Ma_{sub}(< Ma_s)$)†, and it corresponds to hexagons with the fluid rising in the centre of the cell if $\alpha > 0$ (l-hexagons), and to hexagons with the fluid descending in the cell centre if $\alpha < 0$ (g-hexagons). The labelling of the different types of hexagonal convection cells reflects the situation in the Rayleigh convection in a non-Boussinesq fluid where the particular type of convection cells depends on the sign of the kinematic viscosity dependence on temperature (Palm 1960) typical of liquids ($\partial\nu/\partial T < 0$, l-hexagons) or of gases ($\partial\nu/\partial T > 0$, g-hexagons). In this section we consider some of the characteristics of the hexagonal convection pattern in the case when the deformational mode is not excited, i.e. when $Ma_s < Ma_l$ and $H \equiv 0$.

The extent of the subcritical region of a hexagonal Marangoni convection planform has been studied both experimentally (Koschmieder & Biggerstaff 1986; Schatz *et al.* 1995), and theoretically (Scanlon & Segel 1967; Kuznetsov & Spector 1980; Cloot & Lebon 1984; Bragard & Lebon 1993; Bestehorn 1993; Thess & Orszag 1995), within the framework of the one-layer approximation. The value of the subcriticality of a regular hexagonal pattern is

$$\epsilon_{sub} = \frac{Ma_{sub} - Ma_s}{Ma_s} = -\frac{\alpha^2}{4(\lambda_0 + 2\lambda_h)\gamma_0 Ma_s}. \tag{5.2}$$

The subcriticality of the hexagonal Marangoni convection pattern in a two-layer liquid–gas system strongly depends on the gas-to-liquid depths ratio. Figure 2 presents this dependence for the silicon oil–air system used in Schatz *et al.*'s (1995) experiments, and for some other liquid–air systems with the same liquid layer depth. The extent of the subcritical region grows considerably with the decrease of the gas gap, and remains almost constant when the air gap exceeds the depth of the liquid layer. This confirms the results of Bestehorn (1994) that demonstrated the increase of the subcritical region with the increase of the Biot number in the steady state within the framework of the one-layer approach.

The subcriticality of the hexagonal Marangoni convection depends on the heat conductivity and the kinematic viscosity of the liquid layer. However, the key parameter is the Prandtl number of the liquid. This is demonstrated in figure 3, which shows the change of the subcriticality that occurs due to the variation of the liquid heat conductivity for fluids with different kinematic viscosities. Varying the kinematic viscosity affects the Prandtl number only, while the heat conductivity affects also the liquid–gas heat transfer. It can be seen that the larger is the Prandtl number, the stronger is the effect of the heat exchange between the liquid and the gas phase. On

† In fact, however, it can be shown that, due to the quadratic terms containing the gradients of the amplitudes in (4.10), a regular hexagonal planform with $k = k_{cr}$ is unstable in a small subcritical interval $(\gamma_{sub}, \gamma_{sub} + \delta_\gamma)$ near the subcritical threshold γ_{sub}, which means that, in fact, the actual subcritical threshold, at which the regular stable hexagonal pattern with $k = k_{cr}$ occurs, is shifted up and becomes $\gamma'_{sub} = \gamma_{sub} + \delta_\gamma > \gamma_{sub}$. For real systems, this shift is, however, very small, $|\delta_\gamma/\gamma_{sub}| \approx 0.01$ (Nuz *et al.* 1997).

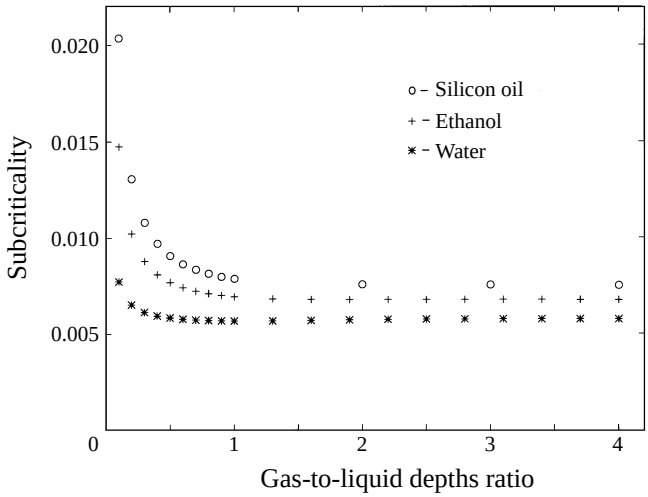

FIGURE 2. The subcriticality of short-scale hexagonal Marangoni convection patterns in different liquid–air systems as a function of the gas-to-liquid depths ratio. Silicon oil data are from Schatz *et al.* (1995) (7.1 cS). In all these systems the threshold of the short-scale Marangoni instability is considerably smaller than the deformational long-scale one.

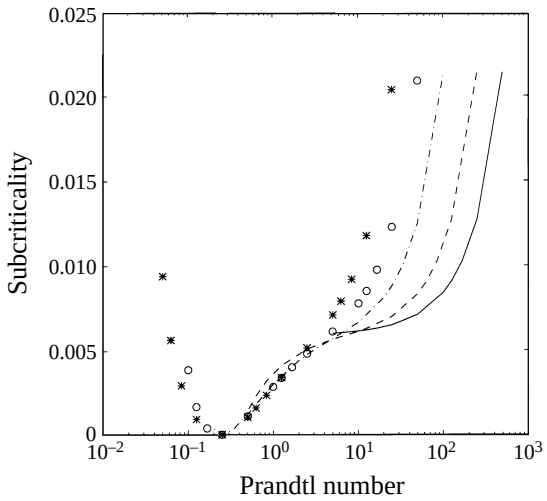

FIGURE 3. The subcriticality of a short-scale hexagonal Marangoni convection in model liquid–air systems as a function of the liquid's Prandtl numbers, for liquids with different kinematic viscosities. Parameters of the liquids: $\rho = 1$ g cm^{-3}, $c_p = 10^7$ erg g^{-1} K^{-1}, $\sigma = 50$ erg cm^{-2}, $\partial\sigma/\partial T = 0.1$ erg cm^{-2} K^{-1}, $L = 1$ mm, $a = 1$; *, $\nu_1 = 0.005$ cm^2 s^{-1}; ○, $\nu_1 = 0.01$ cm^2 s^{-1}; —·—·—, $\nu_1 = 0.02$ cm^2 s^{-1}; — — —, $\nu_1 = 0.05$ cm^2 s^{-1}; ——, $\nu_1 = 0.1$ cm^2 s^{-1}.

the other hand, for liquids with Prandtl number less than that of water, this effect is not particularly important for the value of the subcriticality.

The effect of the heat transfer in the gas phase can also be traced by changing the ratio of heat conductivities and thermal diffusivities. The former characterizes the influence of the conductive heat transfer in the gas phase, while the latter reflects the effect of the gas convection . The dependences of the subcriticality on κ and χ are shown in figure 4 for a hypothetical situation when they are the only

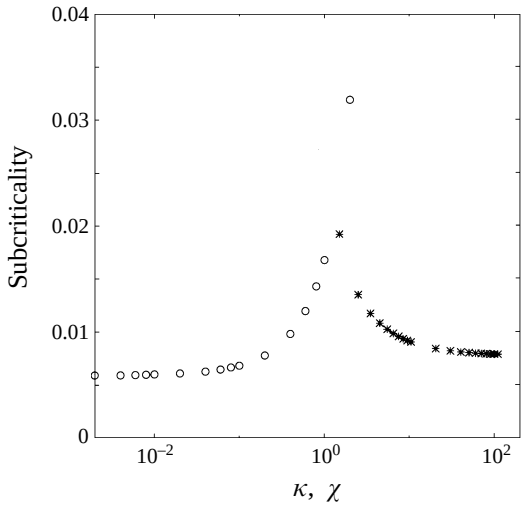

FIGURE 4. The subcriticality of the hexagonal Marangoni convection pattern as a function of the gas-to-liquid ratio of heat conductivities, κ ($\circ$), and of the gas-to-liquid ratio of thermal diffusivities, χ ($*$). All other parameters are those of the silicon oil–air system studied experimentally by Schatz *et al.* (1995).

Liquid	No heat transfer in the gas phase $\kappa = 0,\ \chi = \infty$	Conductive heat transfer in the gas phase $\kappa = \kappa_{air}/\kappa_1,\ \chi = \infty$	Convective heat transfer in the gas phase $\kappa = \kappa_{air}/\kappa_1,\ \chi = \chi_{air}/\chi_1$
Silicon oil, $Pr = 82$	0.58	0.77	0.78
Ethanol, $Pr = 16$	0.56	0.68	0.69
Water, $Pr = 7$	0.53	0.56	0.57
Mercury, $Pr = 0.026$	0.49	0.49	0.79

TABLE 2. The subcriticality (%) of the short-scale hexagonal Marangoni convection in some liquid–gas systems; the geometrical parameters are the same as used by Schatz *et al.* (1995).

variable parameters, all other characteristics being kept constant. Increasing κ (circles) intensifies the conductive heat transfer in the gas phase, while decreasing χ (stars) intensifies the convective heat transport there. It can be seen that the intensification of both types of heat transfer in the gas phase widens the subcritical region of the hexagonal Marangoni convection. The effect of the conductive heat transfer in the gas phase is more pronounced for fluids with a lower heat conductivity. On the other hand, convection in the gas layer has a larger effect on convection in the liquid when the latter has a larger thermal diffusivity.

The effect of the heat transfer in the gas phase on the subcriticality of the short-scale hexagonal convection pattern is illustrated in table 2 which presents the values of the subcriticality for some liquid–gas systems with the same geometrical parameters as those of the silicon oil–air system studied by Schatz *et al.* (1995). It can be seen that for silicon oil and ethanol, having moderate heat conductivities, the effect of the conductive heat transfer in the gas phase is considerable. On the other hand, the effect of convective heat transfer in the gas phase is negligible. This is the reason why the one-layer approach gives correct predictions for convection in these fluids (Van Hook *et al.* 1995). The subcriticality of the hexagonal Marangoni convection pattern in a

water–air system is almost insensitive to the heat transfer in the gas phase due to the large heat conductivity of water. However, for a mercury layer, having large thermal diffusivity, convection in the gas phase has the major effect.

As it can be seen in figure 4 and table 2, the effect of convection in the gas phase is considerable if the gas-to-liquid ratio of thermal diffusivities is about one, or less. Although this situation is not typical of usual experiments in Marangoni convection with high-Prandtl-number fluids, it can be easily met in experiments with liquid metals that are important in eletronic materials processing (Ginde, Gill & Verhoeven 1989). Besides, the thermal diffusivity of the gas layer can be controlled by varying the gas pressure (density): in the ideal gas approximation, the thermal diffusivity and kinematic viscosity of a gas are proportional to its density, while heat conductivity does not depend on it. This fact can provide a good tool for experimental investigation of the effect of convection in the gas phase on Marangoni convection in two-layer liquid–gas systems. For example, in a silicon oil–air system with the air pressure 0.01 atm, the thermal diffusivity of the gas phase will be about the same as the thermal diffusivity of the fluid, and the effect of convection in the gas phase will be significant. (The evaporation of a silicon oil at the room temperature is insignificant even in vacuum (less than one monolayer of molecules per day at room temperature (Williams 1977)), and will not spoil the effect).

The strong dependence of the subcriticality of a hexagonal pattern on the Prandtl number of the fluid demonstrated in figure 3 is caused by the strong dependence of the coefficient of quadratic resonant interaction, α (see (4.6)), on the liquid-phase Prandtl number. Its value Pr_c at which the subcriticality vanishes (see figure 3) corresponds to the change of the sign of α: $\alpha = 0$ at $Pr = Pr_c$. We obtain that $Pr_c \approx 0.22$ is almost the same for a lot of systems with varying viscosities and thermal conductivities. This confirms previous results by Dauby & Lebon (1993), Thess & Bestehorn (1995) and Parmentier, Regnier & Lebon (1996) obtained within the framework of the one-layer approach. If $Pr > Pr_c$, Marangoni convection occurs in the form of l-hexagons, with the fluid rising in the centre of the cell, while in low-Prandtl-number fluids, with $Pr < Pr_c$, it appears in the form of g-hexagons, with the opposite direction of the fluid motion.

As has been shown by Thess & Bestehorn (1995) and Parmentier *et al.* (1996), in one-layer systems the value of Pr_c slightly depends on the Biot number. In real two-layer liquid–gas systems Pr_c depends not only on the parameters a and κ determining the Biot number in the steady state, but also on the parameters χ and v characterizing the effect of convection in the gas phase. Due to this dependence, if the Prandtl number of the liquid layer is close to Pr_c, the transition between l-hexagons and g-hexagons can be induced in experiment, e.g. by varying the gas gap and thus changing the gas-to-liquid depths ratio, or by varying the density (pressure) of the gas and thus changing its thermal diffusivity and kinematic viscosity. This effect, however, can be observed only in specific liquids with $Pr \approx Pr_c$.

6. Pattern selection: hexagons, rolls and squares

In the supercritical region, while the amplitude of the hexagonal Marangoni convection grows, it can become unstable with respect to transitions to patterns with different symmetry – rolls (Scanlon & Segel 1967; Cloot & Lebon 1984; Bragard & Lebon 1993; Bestehorn 1993; Parmentier *et al.* 1996) or squares (Nitschke & Thess 1995; Bestehorn 1996). Such an instability can either occur with respect to infinitesimal perturbations of the amplitudes of the hexagonal pattern, or be induced

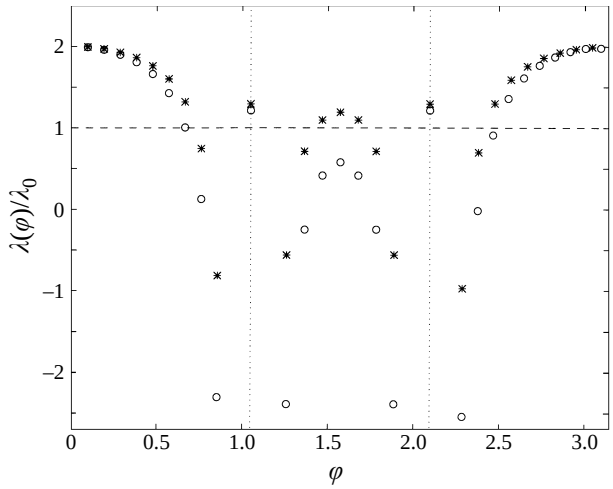

FIGURE 5. Normalized Landau coefficient $\lambda(\varphi)/\lambda_0$ for Marangoni convection in the silicon oil–air system (Nitschke & Thess 1995) (○), and in the water–air system (*). The gas-to-liquid depths ratio is $a = 0.26$, as used in the experiment by Nitschke & Thess (1995).

by finite-amplitude disturbances when another pattern, different from the hexagonal one, becomes energetically preferable.

The thresholds of linear instabilities of the hexagonal pattern, as well as the boundaries dividing energetically preferable patterns, depend on coefficients of nonlinear interaction (the Landau coefficients) between modes at appropriate angles. Besides the coefficient of nonlinear self-saturation, λ_0, and the coefficients of the resonant interaction for hexagons, α and λ_h (see (4.6)), one should know the general Landau coefficient $\lambda(\varphi)$ for $\varphi \neq \pi/3, 2\pi/3$ (Busse 1967; Malomed & Tribelskii 1987).

The hexagons–rolls transition is governed by λ_0 and λ_h, and the hexagons–squares transition is determined by λ_0, $\lambda(\pi/6)$, λ_h and $\lambda(\pi/2)$. What pattern the hexagonal planform will transform to with the growth of the supercriticality depends on the competition between rolls and squares: if $\lambda_0 < \lambda(\pi/2)$ rolls are selected, if $\lambda_0 > \lambda(\pi/2)$ squares are selected (Malomed & Tribelskii 1987; Golovin *et al.* 1995).

The computation of the Landau coefficient $\lambda(\varphi)$ for modes at an arbitrary angle φ is analogous to that described in §4. For $\varphi \neq \pi/3$, $2\pi/3$ this perturbation technique is rigorous since there is no quadratic resonant interaction in this case, and $\lambda(\varphi)$ is computed in the third order of the perturbation theory.

Figure 5 presents the dependence $\lambda(\varphi)/\lambda_0$ for two liquid–gas systems: the silicon oil–air system studied by Nitschke & Thess (1995), and a water–air system with the same depths of the liquid and gas layers. Discontinuities in the dependences correspond to the resonant quadratic interaction at $\varphi = \pi/3, 2\pi/3$; the values of λ_h/λ_0 corresponding to this angle are shown as computed in §4. Note that $\lambda(0) = 2\lambda_0$. It can be seen that for the silicon oil–air system the preferred pattern, except hexagons, is the square one. In the water–air system, far enough from its threshold, the hexagonal pattern will transform to the roll one in this case. For the silicon oil–air systems studied by Nitschke & Thess (1995), the transition between the hexagonal and square convection pattern was observed experimentally.

Figure 6 shows the dependence of $\lambda(\pi/2)/\lambda_0$ on the Prandtl number changing due to varying kinematic viscosity of the liquid layer, for hypothetical fluids with different fixed thermal conductivities. It can be seen that both the liquid Prandtl number

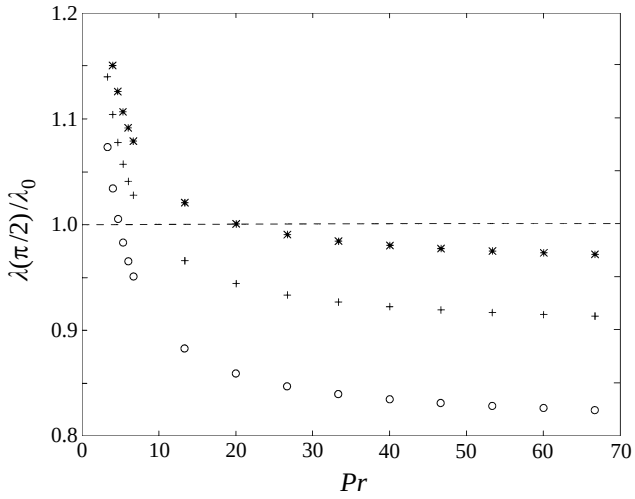

FIGURE 6. Dependence of the normalized Landau coefficient of a square pattern, $\lambda(\pi/2)/\lambda_0$, on the Prandtl number for model liquid–air systems with different heat conductivities of the liquid layer and varying kinematic viscosities. $L = 1$ mm, $a = 0.5$, $\rho = 1\ \mathrm{g\,cm^{-3}}$, $c_p = 10^7\ \mathrm{erg\,g^{-1}\,K^{-1}}$); ○, $\kappa_1 = 1.2\times10^4\ \mathrm{erg\,cm^{-1}\,s^{-1}\,K^{-1}}$; +, $\kappa_1 = 1.5\times10^4\ \mathrm{erg\,cm^{-1}\,s^{-1}\,K^{-1}}$; ∗, $\kappa_1 = 1.8\times10^4\ \mathrm{erg\,cm^{-1}\,s^{-1}\,K^{-1}}$).

and heat transfer between the liquid and the gas layers play an important role in the selection between rolls and squares. There is a clear tendency for the hexagons–squares transition in liquids with larger Prandtl numbers, whereas in liquids with smaller Prandtl numbers the hexagons–rolls transition will occur.

Heat transfer in the gas phase also plays an important role in transition from hexagons to other patterns. This can be seen in figure 7 presenting the dependencies of $\lambda(\pi/2)/\lambda_0$ for the silicon oil–air system used in Nitschke & Thess's (1995) experiment on the gas-to-liquid ratio of heat conductivities. Figure 7 corresponds to a hypothetical situation of large variations of heat conductivity in the gas phase with other parameters being kept constant. As can be seen in figure 7, the effect of conductive heat transfer in the gas layer is considerable and can even lead to subcritical squares. Our computations show that the effect of convection in the gas phase is negligible in this case, due to the large Prandtl number of the silicon oil.

The importance of the heat transfer in the gas phase for the selection of the short-scale Marangoni convection pattern can also be illustrated by the dependence of $\lambda(\pi/2)/\lambda_0$ on the gas-to-liquid depths ratio. Figure 8 shows this dependence for an ethanol–air system (figure 8*a*) and for the silicon oil–air system used by Nitschke & Thess (1995) (figure 8*b*). It can be seen that one can observe either hexagons–rolls or hexagons–squares transitions simply by changing the gas gap.

The calculated Landau coefficients λ_0, λ_h, $\lambda(\varphi)$ allow one to plot a map of transitions between the Marangoni convection planforms which can be observed in the experiment with a particular liquid–gas system. Figure 9 presents such a map for the silicon oil–air system studied by Nitschke & Thess (1995). We have chosen as the map coordinates the two parameters that can be easily varied in experiment: the supercriticality and the gas-to-liquid depths ratio. The solid line marks the subcritical threshold of the Marangoni convection dividing the regions of a quiescent state and a hexagonal pattern (due to rather small subcriticality, the subcritical threshold of the hexagonal pattern almost coincides with the linear one in the scale of this map). The

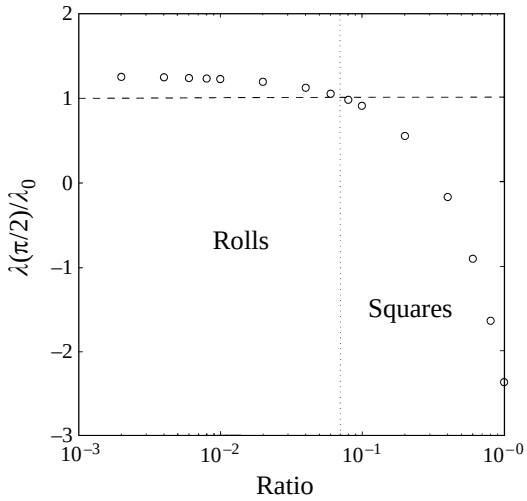

FIGURE 7. Normalized Landau coefficient for the square Marangoni convection pattern $\lambda(\pi/2)/\lambda_0$, for the silicon oil–gas system studied by Nitschke & Thess (1995) as a function of the gas-to-liquid ratio of heat conductivities.

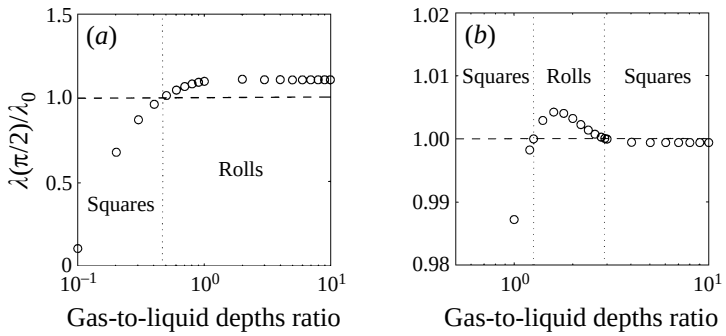

FIGURE 8. Dependence of the normalized Landau coefficient of the square Marangoni convection pattern, $\lambda(\pi/2)/\lambda_0$, on the gas-to-liquid depths ratio for the ethanol–air system (*a*), and for the silicon oil–air system (Nitschke & Thess 1995)(*b*).

dashed lines correspond to the 'first-order' transitions between hexagons and squares or hexagons and rolls: they mark the boundaries where one pattern becomes linearly unstable with respect to the other, and a finite change of the amplitude of the pattern occurs as a result of the transition. The regions between the dashed lines are the bistability regions where hexagons and squares or hexagons and rolls can coexist. The dashed-dotted line is the 'Maxwell line' (where the Lyapunov functions of the two patterns are equal), dividing the bistability regions into two parts where one of the patterns is energetically preferable (the first letter in the region label denotes the preferred pattern). The dotted lines denote the 'second-order' transition between rolls and squares: they mark the boundaries where one of the patterns becomes linearly unstable with respect to the other and, simultaneously, energetically preferable. There is no bistability region for rolls and squares, and the pattern amplitude changes continuously in the course of the transition. It should be mentioned that in this particular silicon oil–air system, hexagons are always linearly stable with respect to squares, and the transition from hexagonal to square convection pattern can result

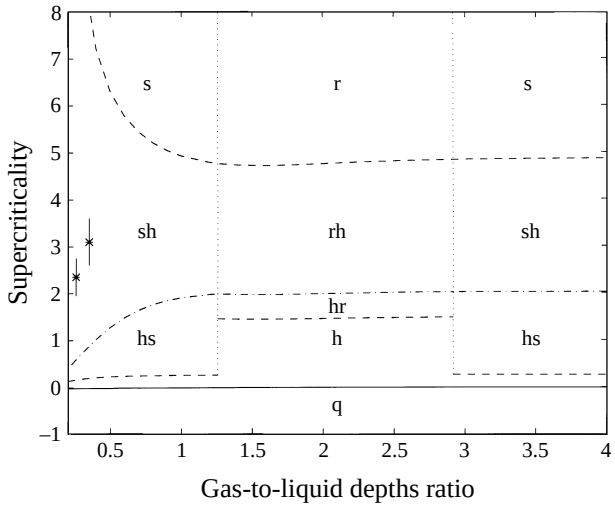

FIGURE 9. Map of the short-scale Marangoni convection patterns which can be observed in the silicon oil–air system studied by Nitschke & Thess (1995): q – quiescent state, h – hexagons, r – rolls, s – squares; hs, sh, and hr, rh – bistability regions of hexagons and squares, and hexagons and rolls, respectively; the first letter denotes the energetically preferable pattern. The stars denote the hexagons–squares transitions experimentally observed by Nitschke & Thess (1995).

only from finite-amplitude disturbances when the square pattern becomes energetically preferable. In the absence of finite-amplitude perturbations, the hexagons in this system will become, at large enough supercriticality, linearly unstable with respect to rolls (the upper dashed line) which, in turn, will transform into squares.

We must note that the Landau coefficients, on the basis of which the boundaries between the patterns are calculated, have been computed at the onset of instability, for $\epsilon \ll 1$. Therefore, the boundaries shown in figure 9 corresponding to $\epsilon > 1$ are, strictly speaking, beyond the applicability of the weakly nonlinear analysis (as well as predictions of previous works summarized by Parmentier *et al.* 1996). However, the present analysis predicts qualitatively the experimentally observed hexagons–squares transition. The experimental results on hexagons–squares transition obtained by Nitschke & Thess (1995) are marked in figure 9 by stars. It can be seen that the theory is in agreement with the experiment. It has been also reported by Nitschke & Thess (1995) that the hexagons–squares transition has a tendency to occur at higher supercriticalities for a more viscous fluid. In a numerical experiment carried out by Bestehorn (1996), it has also been found that the tendency to form regular squares increases with the decrease of the Prandtl number from 10^5 to 50. Our computations confirm this conclusion.

In conclusion of this section we should note that the map of transitions between the patterns with different symmetries presented in figure 9 does not take into account spatial modulations of the patterns and corresponds to patterns with the critical wavelength. Should the pattern wavenumber be different from that corresponding to the band centre, phase instabilities could change the boundaries shown in figure 9. However, our preliminary computations show that spatial modulations at least do not change the threshold of the hexagons–rolls transition at the band centre. The effect of spatial modulations on transitions between different patterns will be described in detail in a forthcoming paper by Nuz *et al.* (1996).

7. Interaction between a short-scale hexagonal convection pattern and a long-scale deformational instability

When the two thresholds of Marangoni instability – the one corresponding to the short-scale hexagonal convection with negligible interfacial deformations and the other corresponding to long-scale deformations of the liquid–gas interface – are close to each other, the nonlinear interaction between these two types of Marangoni convection can yield new secondary instabilities of a hexagonal convection pattern and result in complex non-stationary behaviour.

Let us consider system (4.10) describing the slow long-scale nonlinear evolution of the short-scale hexagonal convection coupled with the evolution of the long-scale surface deformations. We shall dwell here on the case when both modes of the Marangoni convection are excited and $Ma > Ma_{sub} > Ma_l$, i.e. when $\mu > 0$ and $\gamma > \gamma_{sub}$. We shall study the stability of a regular hexagonal pattern with a planar liquid–gas interface, (5.1), with respect to modulating disturbances of the complex amplitudes and of the interfacial deformations in the form of plane waves:

$$\left.\begin{aligned} &A_n = (\rho_0 + \tilde{\rho}_n)\mathrm{e}^{\mathrm{i}\tilde{\phi}_n}, \quad (\tilde{\rho}_n, \tilde{\phi}_n) = (a_n, b_n)\mathrm{e}^{\mathrm{i}(\boldsymbol{q}\cdot\boldsymbol{R}+\omega T)} + \text{c.c.}, \quad n = 1,2,3; \\ &H = \tilde{H} = c\mathrm{e}^{\mathrm{i}(\boldsymbol{q}\cdot\boldsymbol{R}+\omega T)} + \text{c.c.} \end{aligned}\right\} \tag{7.1}$$

where $\rho_0 = \rho_0(\gamma, \lambda)$ is the amplitude of the unperturbed hexagonal pattern given in (5.1), and $\boldsymbol{q}$ and ω are the wave-vector and the complex frequency of the perturbations.

There are two main parameters governing the stability of the hexagonal convection pattern with respect to such disturbances: the parameter γ controlling the amplitude of the hexagons, and the parameter μ, proportional to the difference between the two thresholds $Ma_l - Ma_s$, that controls the growth of surface deformations.

The linear stability analysis of system (4.10) shows that the short-scale hexagonal convection pattern suppresses the deformational instability: when $\gamma > \gamma_{sub} = -1/(4(1 + 2\lambda))$ and the short-scale hexagonal convection exists (see first paragraph of §5), the surface deformation H starts to grow only if μ exceeds a certain threshold μ_{int} depending on γ and other parameters (the details of the linear stability analysis are given in Appendix B).

This deformational instability of a primary regular short-scale hexagonal convection pattern can be either monotonic or oscillatory, and can lead to the development of secondary long-scale stationary deformational patterns or deformational waves propagating along the short-scale hexagonal convection structure and modulating its amplitude and the wavenumber. Figure 10(a, b) shows the neutral stability curves for this secondary deformational instability for the silicon oil–air system studied experimentally by Van Hook *et al.* (1995), where the interaction of the two types of Marangoni convection was first observed.

There are two ways to control this secondary deformational instability. If one changes the depth of the liquid layer and keeps the Marangoni number and the gas-to-liquid depths ratio fixed, then the only varying parameters are the capillary and the Galileo numbers, the latter varying rather strongly, $\sim L_1^3$. Thus, by changing the liquid layer depth, one would strongly affect the linear threshold of the primary long-scale deformational instability, Ma_l, whereas the linear threshold of the primary short-scale instability, Ma_s, would be shifted very slightly at the same time. This would enable one to vary the parameter μ, governing the linear growth of the secondary deformational instability, and at the same time to keep the amplitude of the short-scale convection and, hence, the thresholds of the secondary deformational instability almost constant.

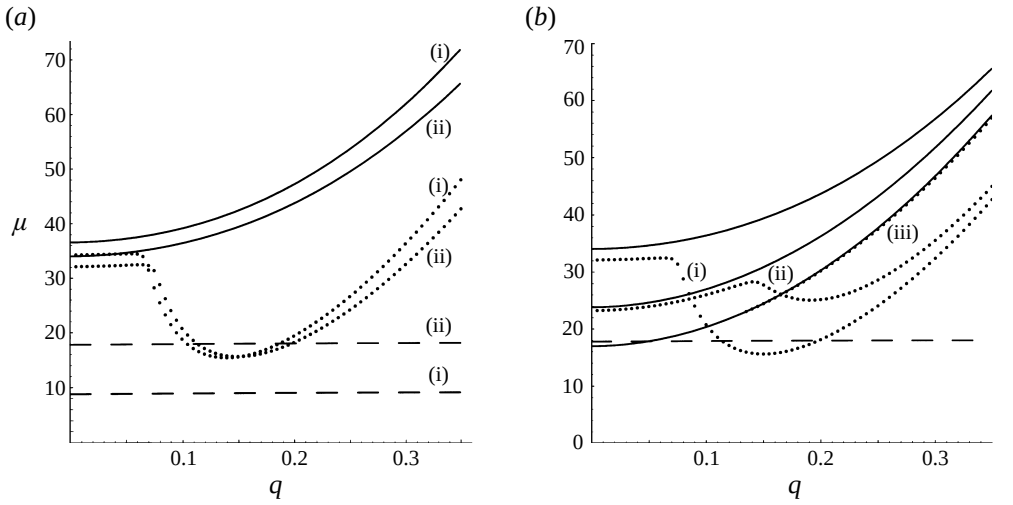

FIGURE 10. Marginal stability curves for the secondary deformational instability of a regular short-scale hexagonal pattern, caused by the interaction with the long-scale deformational mode for the silicon oil–air system studied by Van Hook *et al.* (1995). Solid lines – monotonic instability, dotted lines–oscillatory instability, dashed lines – the values of the parameter μ. (*a*) Varying the liquid layer depth: the Marangoni number and the gas-to-liquid depths ratio are fixed: $Ma = 990$, $a = 1.73$; (i) $L_1 = 0.25$ mm, $\gamma = -0.042$, $w = 375.9$; (ii) $L_1 = 0.22$ mm, $\gamma = -0.035$, $w = 330.8$. Other parameters are: $\lambda = 1.27$, $a_1 = -0.45$, $b_1 = -0.42$, $s_1 = 0.048$, $s_2 = 15.3$. (*b*) Varying the temperature difference: $L_1 = 0.22$ mm, $a = 1.73$; (i) $\gamma = -0.035$ (Ma = 990); (ii) $\gamma = 0.06$ (Ma = 1000); (iii) $\gamma = 1.012$ (Ma = 1100). Other parameters are: $\lambda = 1.27$, $\gamma_{sub} = -0.0705$, $a_1 = -0.45$, $b_1 = -0.42$, $w = 330.8$, $s_1 = 0.048$, $s_2 = 15.33$.

Figure 10(*a*) shows the neutral stability curves for the above-mentioned silicon oil–air system and the parameter μ at different values of the liquid layer depth. If the liquid layer is thin enough, the short-scale hexagonal convection can become unstable with respect to long-scale surface deformations. In the particular case shown in figure 10(*a*), this instability is oscillatory, and leads to the formation of long-scale deformational waves propagating along the hexagonal convection pattern and modulating it. The most dangerous waves are those propagating at the angles of $\pm\pi/6$ with respect to the wave-vectors of the primary short-scale hexagonal structure (the stability curves plotted in figure 10 relate to such system of waves).

Figure 10(*b*) presents the neutral stability curves, corresponding to the same silicon oil–air system, in the case when the thicknesses of the gas and the liquid layers are fixed, and the temperature difference across the system is varied. In this case the parameter μ is fixed and the only variable parameter is γ, growing with the increase of the temperature difference. Its variation leads, in turn, to a variation of the amplitude of the short-scale hexagonal convection and therefore, to a change of the instability curves and the instability thresholds. When the amplitude of the short-scale convection is small, it fails to suppress the deformational instability (at a fixed μ) (see curves (i) in figure 10(*b*)), and the short-scale hexagonal convection undergoes a secondary long-scale oscillatory deformational instability. With the increase of the amplitude of the short-scale convection, the deformational instability gets suppressed, and a stable hexagonal pattern can exist even above the linear deformational instability threshold (figure 10*b*, curves ii). However, a further increase of the amplitude of the short-scale convection destabilizes the system again. In the particular case shown in figure 10(*b*), it undergoes long-scale monotonic deformational instability (figure 10(*b*), curve iii);

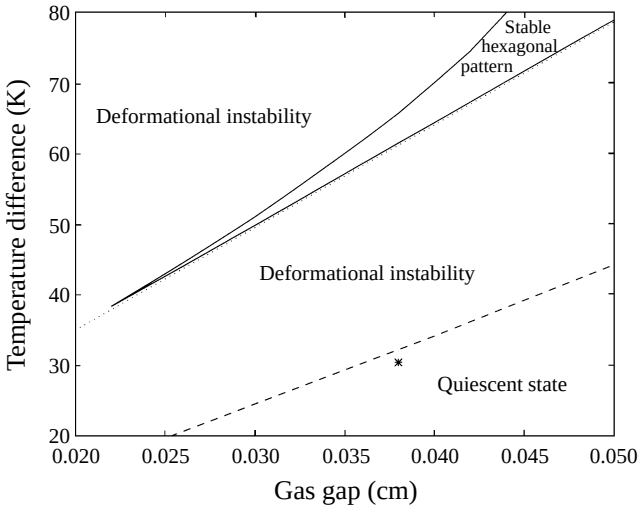

FIGURE 11. Stability diagram for the silicon oil–air system studied by Van Hook *et al.* (1995). The dashed line denotes the linear threshold of the long-scale deformational instability; the dotted line is the subcritical boundary for the short-scale hexagonal convection; solid lines bound the region where the long-scale deformational instability is suppressed by the short-scale hexagonal convection. The star marks the parametric point where the coexistence of the two types of Marangoni instability was observed by Van Hook *et al.* (1995).

at values of the parameters other than those chosen in figure 10(*b*) this secondary instability can also be oscillatory.

Figure 11 shows the map of various instabilities for this silicon oil–air system, at varying values of the temperature difference and the gas gap width L_2. If $L_2 < 0.022$ cm, the short-scale convection can never suppress the deformational instability. When $L_2 > 0.022$ cm, there is a finite interval of temperature differences where the short-scale convection suppresses the deformational instability, and a stable hexagonal convection pattern exists. The lower solid line bounding this region corresponds to the oscillatory deformational instability with $q \neq 0$, i.e. with the characteristic spatial scale of the order of L_1/ϵ, where L_1 is the liquid layer depth, and $\epsilon = (Ma - Ma_s)/Ma_s$ (see curves (i) in figure 10*b*). The upper solid line corresponds to the deformational instability of the short-scale hexagonal convection pattern at $q = 0$, i.e. its characteristic spatial scale is much larger than L_1/ϵ (see curves 3 in figure 10*b*). When $L_2 < 0.038$ cm, this instability is also oscillatory, and at $L_2 > 0.038$ cm it is monotonic. At the cusp point in figure 11, the two thresholds of the secondary deformational instability, at $q \neq 0$ and at $q = 0$, are equal, and at $L_2 < 0.022$ cm both of them are below the fixed value of the parameter μ.

Let us consider in more detail now the secondary oscillatory deformational instability of the short-scale hexagonal convection pattern at $q \neq 0$, which occurs when the lower solid line in figure 11 is crossed. As has been already mentioned, this instability leads to the development of a system of three long-scale (with the wavelength of the order of L_1/ϵ) deformational waves, rotated by $\pi/6$ with respect to the primary hexagonal planform.

In the particular system studied experimentally by Van Hook *et al.* (1995), this instability can occur in a narrow region of temperature differences, between the lower solid line and the adjacent dotted line which marks the subcritical threshold Ma_{sub}

of the short-scale hexagonal convection. For the system geometry for which the two types of Marangoni convection were observed by Van Hook *et al.* (1995) to coexist ($L_1 = 0.22$ mm, $L_2 = 0.38$ mm) this interval is within $\Delta T = 61$–61.4 K.

Below the dotted line $Ma_l < Ma < Ma_{sub}$, and only deformational instability can appear; its linear threshold is shown by the dashed line. In the region between the dashed and the dotted lines, another type of interaction can occur, when the growth of the interfacial deformations generates the short-scale convection under sufficiently large surface elevations. This type of interaction was studied in a one-dimensional case by Golovin *et al.* (1994) and by Kazhdan *et al.* (1995), who have shown it can result in various oscillating, stationary and even chaotic wavy long-scale convective structures (interfacial turbulence). It is most likely that this very interaction has been observed by Van Hook *et al.* (1995) in experiments showing a large, almost dry, spot stabilized by the short-scale hexagonal convection under the elevated liquid film surface. The values of the parameters at which this coexistence of two modes of Marangoni convection was observed by are denoted in figure 11 by a star.

Let us note in conclusion, that some preliminary results of numerical simulation of system (4.10) describing the interaction between the short-scale hexagonal Marangoni convection and the long-scale deformational Marangoni instability, confirm that a long-scale deformational spatio–temporal 'superstructure', resulting from the secondary deformational instability of the primary hexagonal convection pattern and modulating its amplitude, is indeed formed near the instability threshold.

The numerical investigation of strongly nonlinear regimes of the interaction between the two modes of Marangoni convection, both in the case when the two modes are excited and in the case when the excited deformational mode generates the short-scale hexagonal convection, is now in progress, and the results will be published elsewhere.

This work was supported by the Israel Science Foundation. A.A.G. acknowledges the support of the Israel Ministry for Immigrants Absorption. L.M.P. and A.A.N. acknowledge the support by the E. and J. Bishop Research Fund and Minerva Center for Nonlinear Physics of Complex Systems. A.A.N. acknowledges the support by the Fund for Promotion of Research at the Technion. Part of this work was carried out during the visit of A.A.G. and A.A.N. to Instituto Pluridisciplinar, Universidad Complutense de Madrid; we thank Professor M.Velarde for the hospitality and stimulating discussions. We are very grateful to Dr K. Nitschke and to Dr A. Thess from the Dresden University of Technology, and to Dr M. Schatz, Dr S. Van-Hook and Professor E. Koschmieder from the University of Texas at Austin for providing us with the details of their experimental investigations and for fruitful discussions.

Appendix A. Derivation of the evolution equations

The set of linear non-uniform problems appearing in the subsequent orders of the perturbation theory has the following form:

$$\mathscr{L}\boldsymbol{u}^{(i)} = \mathscr{N}^{(i)}[\boldsymbol{u}^{(i-1)}, \boldsymbol{u}^{(i-2)}, \ldots], \tag{A 1}$$

where

$$\mathscr{L} = \begin{pmatrix} (\nabla^2+\partial_{zz})^2 & 0 & 0 & 0 \\ 0 & (\nabla^2+\partial_{zz})^2 & 0 & 0 \\ \beta_0 & 0 & \nabla^2+\partial_{zz} & 0 \\ 0 & \beta_0/(\kappa\chi) & 0 & \nabla^2+\partial_{zz} \end{pmatrix};\ \boldsymbol{u}^{(i)} = \begin{pmatrix} w_1^{(i)} \\ w_2^{(i)} \\ \theta_1^{(i)} \\ \theta_2^{(i)} \end{pmatrix},\ i \geqslant 1, \tag{A 2}$$

and the linear operator $\mathscr{L}$ has the following boundary conditions in the lowest order ($i = 1$):

$$\left.\begin{aligned} &z = 0:\ \ w_1^{(1)} = \partial_z w_1^{(1)} = \theta_1^{(1)} = 0, \\ &z = 1+a:\ \ w_2^{(1)} = \partial_z w_2^{(1)} = \theta_2^{(1)} = 0, \\ &z = 1:\ \ \partial_{zz} w_1^{(1)} - Ma_s \nabla^2 \theta_1^{(1)} = 0, \\ &w_1^{(1)} = w_2^{(1)} = 0,\ \partial_z w_1^{(1)} = \partial_z w_2^{(1)},\ \partial_z \theta_1^{(1)} = \kappa \partial_z \theta_2^{(1)}, \end{aligned}\right\} \tag{A 3}$$

Here $\mathscr{N}^{(i)}[\boldsymbol{u}^{(i-1)}, \boldsymbol{u}^{(i-2)}, \ldots]$ are nonlinear operators generated by the nonlinear and time-dependent terms in the Navier–Stokes and convective heat transport equations, $\mathscr{N}^{(1)} \equiv 0$, $\nabla^2 = \partial_{xx}^2 + \partial_{yy}^2$ is the two-dimensional Laplacian. Equations (A 1) are complemented by corresponding boundary conditions.

The linear problem adjoint to (A 2), (A 3) is

$$\mathscr{L}^* \boldsymbol{u}^* = 0, \tag{A 4}$$

$$\mathscr{L}^* = \begin{pmatrix} (\nabla^2+\partial_{zz})^2 & 0 & \beta_0 & 0 \\ 0 & (\nabla^2+\partial_{zz})^2 & 0 & \beta_0/(\kappa\chi) \\ 0 & 0 & \nabla^2+\partial_{zz} & 0 \\ 0 & 0 & 0 & \nabla^2+\partial_{zz} \end{pmatrix};\ \boldsymbol{u}^* = \begin{pmatrix} w_1^* \\ w_2^* \\ \theta_1^* \\ \theta_2^* \end{pmatrix}, \tag{A 5}$$

$$\left.\begin{aligned} &z = 0:\ \ w_1^* = \partial_z w_1^* = \theta_1^* = 0, \\ &z = 1+a:\ \ w_2^* = \partial_z w_2^* = \theta_2^* = 0, \\ &z = 1:\ \ -\partial_z \theta_1^* + \partial_z \theta_2^* - Ma_s \nabla^2 \partial_z w_1^* = 0, \\ &w_1^* = w_2^* = \partial_z w_2^* = 0,\ \partial_{zz} w_1^* = \partial_{zz} w_2^*,\ \kappa\theta_1^* = \theta_2^*, \end{aligned}\right\} \tag{A 6}$$

where $\boldsymbol{\nabla}$ is the two-dimensional gradient $(\partial_x,\ \partial_y)$. The asymmetry of the adjoint boundary conditions ($\partial_z w_2^* = 0$) stems from the fact that we have neglected the viscous stresses in the gas phase.

The solvability condition for problem (A 1) in the second order is

$$\{\langle \mathscr{N}^{(2)} \cdot \boldsymbol{u}^* \rangle\} = \{\mathscr{M}^{(2)}\}, \tag{A 7}$$

where

$$\mathscr{M}^{(2)} = -[\partial_z w_1^* 2Ma_s \hat{\boldsymbol{\nabla}} \cdot \boldsymbol{\nabla} \theta_1^{(1)}]_{z=1},$$

and $\langle\cdot\rangle$ denotes integration over z-domain, such that

$$\langle f(u_1) + f(u_2) \rangle = \langle f(u_1) \rangle_1 + \langle f(u_2) \rangle_2 = \int_0^1 f(u_1) \mathrm{d}z + \int_1^{1+a} f(u_2) \mathrm{d}z,$$

and $\{\cdot\}$ denotes integration over the periods L_x and L_y of the periodic planform

$$\{\cdot\} = \int_{-L_y}^{L_y} \mathrm{d}y \int_{-L_x}^{L_x} (\cdot) \mathrm{d}x.$$

The solvability condition in the third order reads

$$\{\langle \mathscr{N}^{(3)} \cdot \boldsymbol{u}^* \rangle\} = \{\mathscr{M}^{(3)}\} + H\{\mathscr{F}(1)\}, \tag{A 8}$$

where

$$\mathscr{M}^{(3)} = -[\partial_z w_1^*(2Ma_s\hat{\nabla}\cdot\nabla\theta_1^{(2)} + Ma_s\hat{\nabla}^2\theta_1^{(1)} + Ma_2\nabla^2\theta_1^{(1)})]_{z=1},$$
$$\mathscr{F}(z) = 3\partial_z w_1^{(1)}\nabla^2\partial_z w_1^* + \partial_{zz}w_1^*(\partial_{zz}w_2^{(1)} - \partial_{zz}w_1^{(1)}) + \partial_{zzz}w_1^*\partial_z w_1^{(1)} - \partial_{zzz}w_2^*\partial_z w_2^{(1)}$$
$$-\partial_z w_1^*(-\partial_{zzz}w_1^{(1)} + \nabla^2\partial_z w_1^{(1)} + Ma_s\nabla^2\partial_z\theta_1^{(1)})$$
$$+\theta_1^*(\kappa\partial_{zz}\theta_2^{(1)} - \partial_{zz}\theta_1^{(1)}) - (1/\kappa - 1)\partial_z\theta_2^*\partial_z\theta_1^{(1)},$$

and $w_j^{(1)}$ and $\theta_j^{(1)}$ $(j = 1, 2)$ are the solutions of the linear problem (A 2), (A 3).

Appendix B. Linear analysis of the secondary deformational instability

Substituting the perturbed solutions (7.1) in (4.10), we obtain the following system for the perturbations $\tilde{\rho}$, $\tilde{\phi}$, $\tilde{H}$:

$$\left.\begin{aligned}
\dot{\tilde{\rho}}_n &= \gamma\tilde{\rho}_n + (\boldsymbol{n}_n\cdot\hat{\nabla})^2\tilde{\rho}_n - (3+2\lambda)\rho_0^2\tilde{\rho}_n + (\rho_0 - 2\lambda\rho_0^2)(\tilde{\rho}_l + \tilde{\rho}_m) + \rho_0\tilde{H} \\
&\quad +\rho_0^2\textstyle\sum_{l,m\neq n}(a_1\boldsymbol{n}_l + b_1\boldsymbol{n}_m)\cdot\hat{\nabla}\tilde{\phi}_m, \\
\dot{\tilde{\phi}}_n &= (\boldsymbol{n}_n\cdot\hat{\nabla})^2\tilde{\phi}_n - \rho_0\textstyle\sum_{n=1}^3\tilde{\phi}_n + \sum_{l,m\neq n}(a_1\mathbf{n}_l + b_1\mathbf{n}_m)\cdot\hat{\nabla}\tilde{\rho}_m, \\
\dot{\tilde{H}} &= -\mu\hat{\nabla}^2\tilde{H} - w\hat{\nabla}^4\tilde{H} + 2s_1\rho_0\textstyle\sum_{n=1}^3(\boldsymbol{n}_n\cdot\hat{\nabla})^2\tilde{\rho}_n + 2s_2\rho_0\sum_{n=1}^3\hat{\nabla}^2\tilde{\rho}_n,
\end{aligned}\right\} \tag{B 1}$$

where

$$\rho_0 = \frac{1 + [1 + 4\gamma(1+2\lambda)]^{1/2}}{2(1+2\lambda)}.$$

The dispersion relation for the perturbations is found from the equation

$$\mathrm{Det}(\boldsymbol{M} - \mathrm{i}\omega\boldsymbol{E}) = 0, \tag{B 2}$$

where $\boldsymbol{E}$ is the unit matrix, and

$$\boldsymbol{M} = \begin{pmatrix}
f - n_1^2q^2 & \rho_1 & \rho_1 & 0 & \mathrm{i}\rho_0^2t_{12}q & \mathrm{i}\rho_0^2t_{13}q & \rho_0 \\
\rho_1 & f - n_2^2q^2 & \rho_1 & \mathrm{i}\rho_0^2t_{21}q & 0 & \mathrm{i}\rho_0^2t_{23}q & \rho_0 \\
\rho_1 & \rho_1 & f - n_3^2q^2 & \mathrm{i}\rho_0^2t_{31}q & \mathrm{i}\rho_0^2t_{32}q & 0 & \rho_0 \\
0 & \mathrm{i}t_{12}q & \mathrm{i}t_{13}q & -n_1^2q^2 - \rho_0 & -\rho_0 & -\rho_0 & 0 \\
\mathrm{i}t_{21}q & 0 & \mathrm{i}t_{23}q & -\rho_0 & -n_2^2q^2 - \rho_0 & -\rho_0 & 0 \\
\mathrm{i}t_{31}q & \mathrm{i}t_{32}q & 0 & -\rho_0 & -\rho_0 & -n_3^2q^2 - \rho_0 & 0 \\
h_1q^2 & h_2q^2 & h_3q^2 & 0 & 0 & 0 & \mu q^2 - wq^4
\end{pmatrix},$$

$$f = \gamma - \rho_0^2(3+2\lambda),\ \rho_1 = \rho_0 - 2\lambda\rho_0^2,$$
$$n_1 = \cos\vartheta,\ n_2 = \cos(2\pi/3 - \vartheta),\ n_3 = \cos(2\pi/3 + \vartheta),$$
$$t_{ij} = a_1n_k + b_1n_j\,(k \neq i, k \neq j),\ h_j = -2\rho_0(s_1n_j^2 + s_2),\ i,j,k = 1,2,3,$$

where ϑ is the angle between the perturbation vector $\boldsymbol{q}$ and the x-axis. Setting $\mathrm{Re}(\omega) = \mathrm{Im}(\omega) = 0$ and solving (B 2) with respect to μ yields the neutral stability condition $\mu_s = \mu_s(k; \vartheta, \gamma, \lambda, w, s_1, s_2)$. Setting $\mathrm{Im}(\omega) = 0$, separating the real and imaginary parts in (B 2) and solving the corresponding equations for ω and μ leads to the oscillatory stability boundary $\mu_o = \mu_o(k; \vartheta, \gamma, \lambda, w, s_1, s_2)$.

REFERENCES

BESTEHORN, M. 1993 Phase and amplitude instabilities for Benard–Marangoni convection in fluid layers with large aspect ratio. *Phys. Rev.* E **48**, 3622–3634.

Bestehorn, M. 1994 Pattern selection in Benard–Marangoni convection. *Intl J. Bifurcation and Chaos* **4**, 1085–1094.

Bestehorn, M. 1996 Square patterns in Benard–Marangoni convection. *Phys. Rev. Lett.* **76**, 46–49.

Bragard, J. & Lebon, G. 1993 Non-linear Marangoni convection in a layer of finite depth. *Europhys. Lett.* **21**, 831–836.

Bragard, J. & Velarde, M. 1996, Benard-Marangoni convection: theoretical predictions about planforms and their relative stability. Preprint.

Brand, H. R. 1989 Envelope equations near the onset of a hexagonal pattern. *Prog. Theor. Phys. Suppl.* **99**, 442–449.

Busse, F. H. 1967 The stability of finite amplitude cellular convection and its relation to an extremum principle. *J. Fluid Mech.* **30**, 625–649.

Cloot, A. & Lebon, G. 1984 A non-linear stability analysis of the Benard–Marangoni problem. *J. Fluid Mech.* **145**, 447–469.

Dauby, P. C. & Lebon, G. 1993 Hexagonal Marangoni convection in a rectangular box with slippery walls. *Q. J. Mech. Appl. Maths* **46**, 683–707.

Ginde, R. M., Gill, W. N. & Verhoeven, J. D. 1989 An experimental study of Rayleigh–Benard convection in liquid tin. *Chem. Engng Commun.* **82**, 223–228.

Golovin, A. A., Nepomnyashchy, A. A. & Pismen, L. M. 1994 Interaction between short-scale Marangoni convection and long-scale deformational instability. *Phys. Fluids* **6**, 34–48.

Golovin, A. A., Nepomnyashchy, A. A. & Pismen, L. M. 1995 Pattern formation in large-scale Marangoni convection with deformable interface. *Physica* D **81**, 117–147.

Golovin, A. A., Nepomnyashchy, A. A., Pismen, L. M. & Riecke, H. 1997 Steady and oscillatory side-band instabilities in Marangoni convection with deformable interface. *Physica* D, to appear.

Gunaratne, G. H., Ouyang, Q. & Swinney, H. 1994 Pattern formation in the presence of symmetries. *Phys. Rev.* E **50**, 2802–2820.

Hadji, L. 1994 Non-linear thermal convection in the Benard–Marangoni problem with a free deformable interface. In *Two Fluid Flows – With or Without Phase Change*. ASME AMD vol. 184, pp. 87–94.

Hadji, L. 1996 Non-linear analysis of the coupling between interface deflection and hexagonal pattern in Rayleigh–Benard–Marangoni convection. *Phys. Rev.* E **53**, 5982–5992.

Imaishi, N. & Fujinawa, K. 1974 Theoretical study of the stability of two-fluid layers. *J. Chem. Engng Japan* **7**, 81–86.

Imaishi, N., Fujinawa, K. & Tadaki, T. 1980 Effect of oscillatory instability on stability of two-fluid layers. *J. Chem. Engng Japan* **13**, 360–365.

Kazhdan, D., Shtilman, L., Golovin, A. A. & Pismen, L. M. 1995 Non-linear waves and turbulence in Marangoni convection. *Phys. Fluids* **7**, 2679–2685.

Koschmieder, E. L. & Biggerstaff, M. I. 1986 Onset of surface-tension-driven convection. *J. Fluid Mech.* **167**, 49–64.

Kuznetsov, E. A., Nepomnyashchy, A. A. & Pismen, L. M. 1995 New amplitude equation for Boussinesq convection and non-equilateral hexagonal patterns. *Phys. Lett.* A **205**, 261–265.

Kuznetsov, E. A. & Spector, M. D. 1980 On a weakly supercritical convection. *J. Appl. Mech. Tech. Phys.* **21**, 220–228.

Malomed, B. A. & Tribelskii, M. I. 1987 Stability of stationary periodic structures for weakly supercritical convection and related problems. *Sov. Phys. JETP* **65**, 305–310.

Newell, A. C. & Whitehead, J. A. 1969 Finite bandwidth, finite amplitude convection. *J. Fluid Mech.* **38**, 279–303.

Nitschke, K. & Thess, A. 1995 Secondary instability in surface-tension-driven Benard convection. *Phys. Rev.* E **52**, R5772–R5775.

Nuz, A., Golovin, A. A., Nepomnyashchy, A. A. & Pismen, L. M. 1997 New types of secondary instabilities of hexagonal patterns. In preparation.

Palm, E. 1960 On the tendency towards hexagonal cells in steady convection. *J. Fluid Mech.* **8**, 183–192.

Parmentier, P. M., Regnier, V. C. & Lebon, G. 1996 Non-linear analysis of coupled gravitational and capillary thermoconvection in thin liquid layers. *Phys. Rev.* E **54**, 411–423.

Pismen, L. M. & Nepomnyashchy, A. A. 1993 Structure of dislocations in the hexagonal pattern. *Europhys. Lett.* **24**, 461–465.

Pomeau, Y. 1986 Front motion, metastability and subcritical bifurcation. *Physica* D **23**, 3–11.

Pontes, J. R. M. 1994 Pattern formation in spatially ramped Rayleigh–Benard systems. PhD Thesis, Universite Libre de Bruxelles.

Reichenbach, J. & Linde, H. 1981 Linear perturbation analysis of surface tension driven convection at a plane interface (Marangoni instability). *J. Colloid Interface Sci.* **84**, 433–443.

Scanlon, J. W. & Segel, L. A. 1967 Finite-amplitude cellular convection induced by surface tension. *J. Fluid Mech.* **30**, 149–162.

Schatz, M. F., Van-Hook, S. J., McCormic, W. D., Swift, J. B. & Swinney, H. 1995 Onset of surface-tension-driven Benard convection. *Phys. Rev. Lett.* **75**, 1938–1941.

Segel, L. E. 1969 Distant side-walls cause slow amplitude modulation of cellular convection. *J. Fluid Mech.* **38**, 203–224.

Simanovskii, I. B. & Nepomnyashchy, A. A. 1993 *Convective Instabilities in Systems with Interface*. Gordon and Breach.

Smith, K. A. 1966 On convective instability induced by surface tension gradients. *J. Fluid Mech.* **24**, 401–414.

Takashima, M. 1981 Surface tension driven instability in a horizontal liquid layer with a deformable free surface. *J. Phys. Soc. Japan* **50**, 2745–2750.

Thess, A. & Bestehorn, M. 1995 Planform selection in Benard-Marangoni convection: *l*-hexagons versus *g*-hexagons. *Phys. Rev.* E **52**, 6358–6367.

Thess, A. & Orszag, S. A. 1995 Surface-tension-driven Benard convection at infinite Prandtl number. *J. Fluid Mech.* **283**, 201–230.

Van-Hook, S. J., Schatz, M. F., McCormic, W. D., Swift, J. B. & Swinney, H. 1995 Long-wave instability in surface-tension-driven Benard convection. *Phys. Rev. Lett.* **75**, 4397–4400.

Williams, R. 1977 The advancing front of a spreading liquid. *Nature* **266**, 153–154.